Catalysis Science & Technology

Unravelling the Metal-Support Interactions in χ-Fe5C2/MgO Catalysts for Olefins Synthesis Directly from Syngas

Journal:	*Catalysis Science & Technology*
Manuscript ID	CY-ART-11-2021-002022.R1
Article Type:	Paper
Date Submitted by the Author:	03-Dec-2021
Complete List of Authors:	Liu, Yitao; East China University of Science and Technology School of Chemical Engineering Liu, Xianglin; East China University of Science and Technology School of Chemical Engineering Yang, Zixu; East China University of Science and Technology School of Chemical Engineering Li, Hu; East China University of Science and Technology School of Chemical Engineering Ding, Xiaoxu; East China University of Science and Technology School of Chemical Engineering Xu, Minjie; East China University of Science and Technology School of Chemical Engineering Li, Xinli; Zhengzhou University Tu, Wei-feng; Zhengzhou University Zhu, Minghui; East China University of Science and Technology School of Chemical Engineering Han, Yifan; East China University of Science and Technology School of Chemical Engineering

ARTICLE

Unravelling the Metal-Support Interactions in χ-Fe_5C_2/MgO Catalysts for Olefins Synthesis Directly from Syngas

Received 00th January 20xx,
Accepted 00th January 20xx

DOI: 10.1039/x0xx00000x

Yitao Liu [a], Xianglin Liu [a], Zixu Yang [a], Hu Li [a], Xiaoxu Ding [a], Minjie Xu [a], Xinli Li [b], Wei-Feng Tu [b], Minghui Zhu [a] and Yi-Fan Han [a, b, *]

We reported the χ-Fe_5C_2/MgO catalyst for olefins synthesis directly from syngas (STO), showing high selectivity to C_2-C_4 olefins and catalytic stability. With characterization of morphology, electronic structures, and adsorption/desorption properties using in/ex situ techniques (XPS, TEM, XRD, MES, PHTA and TPD), we revealed that MgO could perform not only as a structural promoter to disperse active iron phase and prevent the particle agglomeration during the reaction, but also an electronic modifier to transfer electrons to iron. Especially, in combination of spectroscopy and theory calculations, we have proved that the close intimacy between χ-Fe_5C_2 and MgO (~0.3 electrons-transfer from MgO to χ-Fe_5C_2) enhanced CO dissociative adsorption whilst weakening the secondary hydrogenation of olefins, leading to the enhancement of selectivity. The dual roles of MgO in χ-Fe_5C_2/MgO may shed light upon rational design of practical STO catalysts by taking advantages of the exceptional strong metal-support interactions (SMSIs).

1. Introduction

Lower olefins, e.g., ethylene, propylene and butylene are building blocks for producing composites and fine chemicals ranging from plastics, drugs, dyes to cosmetics, detergents, lubricant and so on.[1] Currently, olefins are mainly produced from steam cracking of a broad range of hydrocarbon feedstocks (e.g. naphtha, gas oil, and condensates), dehydrogenation of light paraffin, and by-products of refining processes.[2] Considering the depleting of fossil resources and growing public concerns on low-carbon economics, intensive efforts have been made to develop alternative approaches for olefins production using non-petroleum feedstocks via syngas ($CO+H_2$), which could come from biomass, CO_2 reduction and dry gas reforming, etc. Indirect strategies like methanol/dimethyl ether to olefins (MTO/DMTO) have been successfully developed and commercialized.[3, 4] Meanwhile, the direct conversion of syngas to olefins process (STO) becomes an attractive route, which avoids the step of intermediates (e.g., methanol, dimethyl ether, etc.) formation, allowing for lower energy input, water consumption and capital investment compared to MTO. Thus, the STO process has gained increasing attention in recent decades. Up till now, the key challenge of this technology is the development of industrial catalysts with high selectivity at a long-time durability.[5, 6]

Iron (Fe) is one of the active metals for STO because of its vast availability, flexibility to H_2/CO ratio associated with its high water-gas shift activity, poison-resistance and high selectivity to olefins.[7, 8] The product distribution of STO is subject to the Anderson-Schultz-Flory (ASF) distribution, which predicts that the maximal selectivity to C_2-C_4 olefins is about 58%.[9, 10] The relative harsh reaction conditions (250-350 °C, 1.0-3.0 MPa) cause catalysts deactivation quickly.[11] It has found that the selectivity and stability of catalysts can be improved by decorating the active metals with structural and electronic promoters.[2]

In the catalyst pelleting process, structural promotors/supports, such as SiO_2 and Al_2O_3, are typically used for dispersing and stabilizing the active phase because of their excellent mechanical and hydrothermal stability. However, the strong interactions between the iron oxides and supports are likely to hinder the reduction and carbonization of iron oxides,[12, 13] thus compromising the olefin selectivity. For instance, Suo et al. reported that the formation of Fe-O-Si inhibited the reduction and activation of catalysts.[12] Similarly, Wan et al. reported that Fe-Al_2O_3 interactions weakened surface basicity of catalysts, thus stabilizing the FeO phase and delaying the reduction and carburization.[13]

Electronic promotors, such as alkali metals (Na and K), are generally employed as the electron donors to improve the adsorption/dissociation of CO and avoid the secondary hydrogenation to boost olefin selectivity. However, excessive CO adsorption/dissociation induced by alkali metals tends to favour the carbon deposition on the surfaces of catalysts.[11, 14, 15] Consequently, the stability of the catalyst is crippled. Cheng et al. mentioned that the high content of K tended to enlarge

[a] State Key Laboratory of Chemical Engineering, East China University of Science and Technology, 130 Meilong Road, Shanghai 200237, China
[b] Engineering Research Center of Advanced Functional Material Manufacturing of Ministry of Education, Zhengzhou University, Zhengzhou, 450001, China
Electronic Supplementary Information (ESI) available: [details of any supplementary information available should be included here]. See DOI: 10.1039/x0xx00000x

the size of iron carbides and block the active sites by K-induced carbon deposition.[15]

Based on the argument of the impacts of the structural and electronic promotors on the catalytic performance, it seems that there is a trade-off between product selectivity and catalytic stability. In this study, we prepared a highly dispersed iron catalysts supported on MgO, which is expected to improve both C_2-C_4 olefin selectivity and long-time stability. As an alkaline earth metal oxide, MgO is widely used as a solid base catalyst for catalysing isomerization, aldol condensation, Knoevenagel condensation, Si-C bond formation and so on.[16, 17] MgO has also been added to improve the surface basicity of the iron-based STO catalysts to promote the catalytic performance.[18-20] However, the decorating roles of MgO on active phase can be hardly elucidated in such a complex system due to unresolved interactions between Fe and MgO. Moreover, owing to its excellent thermal stability, MgO is extensively used in manufacturing of refractory materials,[21, 22] being an ideal carrier to stabilize the active phase in harsh conditions. To the best of our knowledge, studies on MgO supported iron catalysts for the STO reaction have been scarcely reported so far. To bridge this gap, a comparative study is performed to examine the unique properties of MgO in decorating the structural and electronical features of the active iron carbides in χ-Fe_5C_2/MgO. A series of in/ex situ characterization techniques combined with Density Function Theory (DFT) calculation were carried out to study the structure-activity relationship.

2. Experimental and methods

2.1 Catalyst Preparation

Preparation of Fe_2O_3/MgO. 15wt% Fe_2O_3/MgO catalyst precursor was prepared by an incipient wetness impregnation method. Typically, 1.08 g $Fe(NO_3)_3{\cdot}9H_2O$ (Aladding, 99.99%) was dissolved by 1000 μL deionized water. Subsequently, the above solution was added drop by drop to 1.0 g MgO (Adams-beta, 97+%) under simultaneous stirring until the required pore volume of MgO powder was attained. The resulting precipitates aged under stagnant air at room temperature for about 12 hours, then filtrated and dried under vacuum at 60 °C for overnight. The dried mixture was grinded, calcinated in a muffle furnace at 450 °C for 4 hours with a ramping rate of 2 °C /min, and then cooled to room temperature to afford final solid as Fe_2O_3/MgO. To evaluate the critical role of the catalyst support, two different samples of iron oxide, powder mixed with MgO (p-Fe_2O_3-MgO) and with SiC (p-Fe_2O_3-SiC), were prepared as reference catalysts. Briefly, p-Fe_2O_3-MgO/p-Fe_2O_3-SiC were made by mixing the Fe_2O_3 powder and MgO/SiC powder with a mass ratio of 3:11 (thus making a 15wt% Fe content), respectively. The phase and particle size of the physically mixed fresh iron catalysts are kept at the same level as that of Fe_2O_3/MgO.

Preparation of Fe_2O_3/MgO with controlled Fe_2O_3-MgO intimacies. Catalysts with controlled Fe_2O_3-MgO intimacies were prepared by physical motor mixing MgO and Fe_2O_3. It notes that the phase and particle size of the physically mixed fresh iron catalysts are kept at the same level as that of Fe_2O_3/MgO. The Fe_2O_3 intimacies were adjusted by mixing MgO or SiC and Fe_2O_3 with different meshes. The mass ratio of Fe_2O_3 and MgO/SiC was 3:11, thus making a 15wt% Fe content. Briefly, p-Fe_2O_3-MgO/p-Fe_2O_3-SiC were made by mechanical mixing Fe_2O_3 powder and MgO/SiC powder. m-Fe_2O_3-MgO/g-Fe_2O_3-MgO were prepared by mechanical mixing pelleted MgO and Fe_2O_3 at 160~200 meshes/20~40 meshes, respectively. It is obvious that the proximities of Fe_2O_3 and MgO for different precursors take on an order of Fe_2O_3/MgO > p-Fe_2O_3-MgO > m-Fe_2O_3-MgO > g-Fe_2O_3-MgO >> p-Fe_2O_3-SiC.

Preparation of MgO/Fe_2O_3 with different MgO loadings. MgO/Fe_2O_3 catalysts were prepared by an incipient wetness impregnation method. Typically, 0.53 g $Mg(NO_3)_2{\cdot}6H_2O$ (Adamas, 99+%) was dissolved by 5.0 mL deionized water. Subsequently, the above solution was added drop by drop to 1.0 g Fe_2O_3 under simultaneous stirring until the required pore volume of Fe_2O_3 powder was attained. The mixture was stirred to be dried. Then, the residue solution was repeatedly added with the same procedure. The resulting precipitates aged under stagnant air at room temperature for about 12 hours, then filtrated and dried under vacuum at 60 °C for overnight. The dried mixture was ground, calcinated in a muffle furnace at 450 °C for 4 hours with a ramping rate of 2 °C/min, and then cooled to room temperature to afford final solid as 5MgO/Fe_2O_3. 10MgO/Fe_2O_3 and 20MgO/Fe_2O_3 were prepared by varying $Mg(NO_3)_2{\cdot}6H_2O$ at 1.06 g/2.12 g while keeping the others unchanged.

Labels of the spent catalysts. It should be noted that the iron phase in all the as-prepared precursors is Fe_2O_3, and the active phase is χ-Fe_5C_2, which will discussed and proved in **3. Results and discussion**. Thus, all "Fe_2O_3" denoted in the fresh precursors will be substituted as "χ-Fe_5C_2" in the corresponding spent catalysts. For example, the as-synthesized "Fe_2O_3/MgO" will re- labelled as "χ-Fe_5C_2/MgO".

2.2 Activity Measurements

The reaction was performed under industrially relevant conditions of 280 °C, 2.0 MPa and a H_2/CO/N_2 ratio of 45/45/10 (25 mL/min) in a fixed-bed micro-reactor with a 6 mm inner diameter stainless steel tube inside. Prior to the reaction, the catalyst precursor (100 mg) was activated online by 5% H_2/5% CO/N_2 (30 ml/min) at 350 °C, 0.1 MPa for 5 h. After cooling the reactor temperature to 150 °C in Ar flow, the reaction system was pressurized with the reactants (45% H_2/45% CO/N_2) to 2.0 MPa over the as-activated catalysts. Subsequently, the temperature was increased to 280 °C with a ramping rate of 1 °C/min. It is noted that the active iron carbide, χ-Fe_5C_2, was formed during this process.

The products were detected online by a gas chromatography (Shanghai Ruimin GC2060). Hydrocarbon was analysed by the capillary column (Agilent HP-Plot Q) with a hydrogen flame ionization detector (FID). H_2 and N_2 were analysed by a 5A

molecular sieve column with a thermal conductivity detector (TCD) while CO and CO_2 were analysed by a TDX-01 column with an FID coupled with a methane reformer. Product selectivity is determined on a carbon basis. The carbon balances of involved reactions were over 96%. Spent catalysts were passivated using 1% O_2/N_2 before unloaded from the reactor and kept in a vacuum chamber for further characterization.

CO conversion (XCO) and product selectivity are calculated as **Eqs.1-2**:

$$X_{CO} = \frac{Q_{in}\upsilon_{CO,in} - Q_{out}\upsilon_{CO,out}}{Q_{in}\upsilon_{CO,in}} * 100\% \quad (1)$$

Q_{in}: Total inflow rate, mL/ min.

Q_{out}: Total outflow rate, mL/min.

$\upsilon_{CO,in}$: the concentration of CO in the inflow.

$\upsilon_{CO,out}$: the concentration of CO in the outflow.

$$\text{Selectivity}\ (\%) = \frac{nC_i}{\Sigma nC_i} \times 100\% \quad (2)$$

n: carbon number of corresponding products.

C_i: concentration of corresponding products.

2.3 Characterization

Transmission electron microscope (TEM) images were captured at FEI Tecnai G2 with 200 kV accelerating voltage. After grinding and ultrasonic dispersing in anhydrous ethanol, few drops of the slurry were dripped on ultrathin carbon film coated copper grids and dried under an infrared lamp prior to the measurement. The size distribution of iron compounds was determined based on more than 200 particles.

Quasi in-situ XPS characterization was conducted on a Custom-made SPECS spectrometer equipped with a monochromatic Al-K radiation source (1486.6 eV, pass energy 20.0 eV). Before transferring to ultrahigh vacuum chamber for testing activated catalysts, the samples were pre-treated by 1% CO/Ar at 350 °C for 5h in the treated chamber. And then, the activated samples were back to the treated chamber for reaction process. The reaction conditions were 280 °C, 2.0 MPa, and a $H_2/CO/N_2$ ratio of 45/45/10 (25 mL/min) for 3 hours. The used catalysts were transferred to the measurement chamber under vacuum environment. The binding energies (BEs) of Fe and Mg elements were calibrated by setting C1s peak at 284.8 eV as reference.

X-ray powder diffraction (XRD) patterns were collected at a Bruker D8 Advance diffractometer sourced by a monochromatic Cu-Kα radiation (λ=1.5418 Å) with continuous scanning angle (2θ) from 10° to 80° along with 40 kV accelerating voltage, 40 mA detecting current.

Mössbauer spectroscopy (MES) experiments were conducted on a Wissel 1550 electromechanical spectrometer sourced by a 57Co/Pd irradiation at room temperature under a constant acceleration transmission mode. The least-squares fitting method was adopted for the fitting of the spectra.

Temperature-programmed desorption of CO, H_2, C_3H_6 (CO, H_2, C_3H_6-TPD) and pulse-C_3H_6 hydrogenation transient analysis (PHTA) were conducted in a micro fixed-bed reactor (Linkam Scientific Instruments Ltd.) coupled with a mass spectrum detector (MSD) (HPR-20, Hiden Analytical Ltd.) to analyse the desorbed compounds. All of adsorbates were diluted with 90% Ar unless otherwise specified. For the TPD measurements, 50 mg of 20 h-spent sample was re-activated by 5% H_2/5% CO/Ar for 5 hours at 350 °C with 5 °C/min heating ramp and cooled to room temperature in Ar flow. After exposure to adsorbate for 1 hour, the catalyst was switched to Ar flow until the baseline of the adsorbate signal in MS was levelled off. The desorption process was performed by increasing the temperature from room temperature to 800 °C at a ramping rate of 10 °C /min. For the PHTA experiments, 50 mg of 20 h-spent sample was re-activated by 5% H_2/5% CO/Ar for 5 hours at 350 °C with 5 °C/min heating ramp and cooled to room temperature in Ar flow. The pulse-C_3H_6 hydrogenation process was carried out at 280 °C. H_2 and C_3H_6 flow were controlled by a six-way valve equipped with a 1 mL quantitative loop. H_2 was continuously purged while C_3H_6 was pulsed in every 3 minutes held for 5 seconds. The signals of C_3H_6 and corresponding C_3H_8 were recorded by an MSD.

2.4 Computational Methods

Periodic density functional theory (DFT) calculations were performed using the Vienna ab initio simulation package (VASP).[23, 24] The exchange-correlation energy of electrons was treated with the generalized gradient approximation (GGA) parameterized by the Perdew-Burke Ernzerhof (PBE).[25] The electron-ion interactions were described by the projector augmented wave (PAW) method. A cut-off energy of 400 eV was selected for the plane-wave expansion. The convergence criteria for the force and electronic self-consistent iteration were set to 0.05 eV/Å and 10-5 eV, respectively. Bader charge analysis was used to investigate the electron transfer phenomena.

The bulk structures of χ-Fe_5C_2 and MgO were fully relaxed during the calculations. The optimized lattice constants were a = 11.56, b = 4.51, c = 4.99 Å for χ-Fe_5C_2; and a = b = c = 4.21 Å for MgO, consistent with other theoretical studies.[26-29] A 3 × 3 MgO (001) surface with a χ-Fe_5C_2 cluster comprising 5 iron and 2 carbon atoms (χ-Fe_5C_2/MgO (001)) was used to simulate χ-Fe_5C_2/MgO catalyst (Supporting Information (SI), Figure S1a and Figure S1b). The top two layers of MgO, χ-Fe_5C_2 cluster and adsorbates were relaxed in all calculations. To explore the effects of MgO supporter on C_3H_6 adsorption on χ-Fe_5C_2 surface, crystal orbital Hamilton population (COHP) analyses were performed. For C_3H_6 adsorption, a 2 × 1 χ-Fe_5C_2 (510) surface was built for comparison (Figure S1c and Figure S1d). For the χ-Fe_5C_2 (510) model, the bottom 11 Fe layers and 5 C layers (22 Fe + 10 C) were fixed at their bulk positions, while the top 12 layers (18 Fe + 6 C) and adsorbates were allowed to relax. A Gamma-centred (1 × 1 × 1) K mesh was used in all calculations. In all the slab models, vacuum layers of 20 Å were applied to avoid the interactions among slabs in the z direction.

3. Results and discussion

3.1 Structure of Fe_2O_3/MgO

STO has been recognized as a highly phase-sensitive[30, 31] and size-dependent[32, 33] reaction. In this study, the phase and size of iron species for all as-prepared precursors are controlled at the same level to rule out the effects of phase and size on the catalytic performance. XRD patterns (Fig. S2) reveal that no features of iron species but only peaks corresponding to MgO are observed for Fe_2O_3/MgO, indicating that iron species are highly dispersed on MgO. Similarly, Lee et al.[34] reported that diffraction peaks of iron species were undetectable if the Fe loading amount was less than 30 wt% in Fe_2O_3/MgO. MgO has showed great ability in dispersing other active metals as well. For instance, Zhang et al.[35] showed that the diffraction peaks of Co_3O_4 were identifiable when cobalt was supported on Al_2O_3, SBA-15 and ZnO but not on MgO. They attributed the excellent dispersion of Co to the surface basicity of MgO.

The phase composition of those precursors was also examined using MES. The doublet with 0.32 mm/s isomer shifts (I.S.) and 0.68 mm/s quadrupole splitting (Q.S.) (Fig. 1a and Table S1) demonstrated the formation of Fe_2O_3.[36] Moreover, the absence of hyperfine field (Hhf) signal related to super-paramagnetic indicates that the particle size of Fe_2O_3 is smaller than the critical size (13.5 nm).[36] TEM images also show that iron species are highly dispersed on MgO (Fig. S3a). The average particle size of iron was measured to be 8.1 ± 1.8 nm (Fig. S3b). α-Fe_2O_3 crystal along zone axis [4 -4 1] was identified according to the HR-TEM image (Fig. S3c) and its fast Fourier transformation (FFT) (Fig. S3d) results. Thus, it is concluded that the iron phase in Fe_2O_3/MgO was dominated by α-Fe_2O_3 with a particle size of 8.1 nm. With this acknowledgement, we subsequently prepared the powder mixed iron-based catalysts (p-Fe_2O_3-MgO and p-Fe_2O_3-SiC) using a commercial α-Fe_2O_3 with a particle size of 10 nm (US Research Nanomaterials, Inc.) as descripted in the catalyst preparation section.

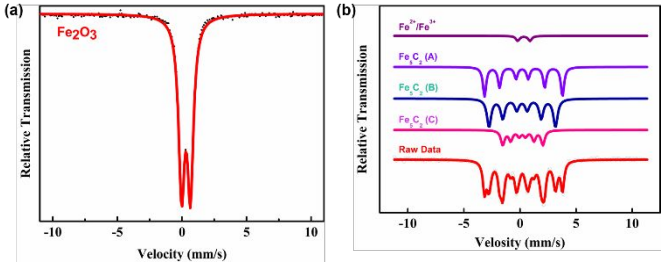

Fig. 1 Mössbauer spectra for (a) Fe_2O_3/MgO (precursor) and (b) χ-Fe_5C_2/MgO (50 h-spent catalysts).

3.2 Catalytic Performance

Catalytic activity and product selectivity were summarized in Table 1. The conversions of CO over all catalysts were controlled at ca. 23% for selectivity comparison. The χ-Fe_5C_2/MgO catalyst exhibited the highest selectivity of 56.9% to C_2-C_4 olefins and the ratio of olefin to paraffin (5.3) among all catalysts, which outperforms most of the supported reported iron-based catalysts operated under typical STO practice (Table S2). Notably, the p-Fe_2O_3-MgO prepared by physically mixing α-Fe_2O_3 (particle size: 10 nm) and MgO shows a C_2-C_4 olefins selectivity of 52.7%, manifesting that the proximity between active iron phase and MgO significantly affects the catalytic performance. The lowest olefin selectivity (40.4%) was obtained for p-Fe_2O_3-SiC, which hinted that the strong metal support interactions (SMSIs) effect induced by MgO favoured the formation of olefins.

Table 1 Catalytic performance of χ-Fe_5C_2/MgO, p-χ-Fe_5C_2-MgO and p-χ-Fe_5C_2-SiC

Catalyst	CO Conversion (%)	Selectivity with CO_2 excluded (%)							CO_2 selectivity	Olefin/Paraffin		Carbon Balance (%)
		CH_4	$C_2^=$	$C_3^=$	$C_4^=$	C_{5+}	Oxygenates	C_2-$C_4^=$		C_3	C_2-C_4	
χ-Fe_5C_2/MgO	20.8	23.6	14.9	26.3	15.7	8.7	0.1	56.9	38.4	8.2	5.3	98.3
p-χ-Fe_5C_2-MgO	23.0	25.9	14.4	23.9	14.4	8.0	1.1	52.7	41.5	8.0	4.3	99.1
p-χ-Fe_5C_2-SiC	24.6	32.6	13.7	20.8	7.9	7.4	0.9	40.4	45.3	4.3	2.2	98.5

Reaction conditions: 100 mg of catalyst, 280 °C, 2.0 MPa, 25 mL/min, H_2/CO = 1. Reaction time: 20 h. The GHSV were controlled to make sure CO conversions of different catalysts were comparable since the product selectivity of Fischer-Tropsch synthesis could be affected by CO conversion.

3.3 MgO as an electronic promoter

Electronic structures. The electronic structure of catalyst is universally regarded as the key factor steering the selectivity in heterogeneous catalysis.[37-41] Typical XPS spectrum of iron carbides (Fig. 2a) were observed with a spin-coupled doublet for Fe 2p3/2 and Fe 2p1/2 at about 707.7 and 720.9 eV, respectively.[42, 43] While the binding energy (BE) for the corresponding peaks of Fe in χ-Fe_5C_2/MgO downshifts by 0.4 eV compared to those of Fe_2O_3. In contrast, the BE of Mg 2p is 0.3 eV higher for χ-Fe_5C_2/MgO than that of pure MgO (Fig. 2b). The rise of electron density of Fe together with a drop in electron density of MgO speculated from the BE variation indicates the electron transfer from MgO to χ-Fe_5C_2.

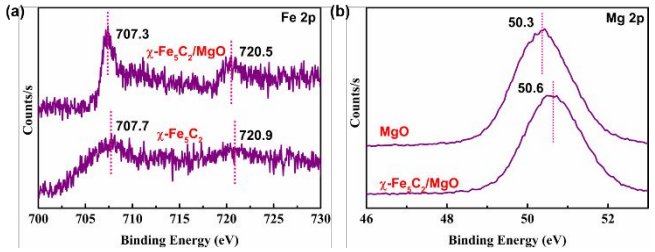

Fig. 2 (a) Quasi in-situ Fe 2p XPS spectra of χ-Fe_5C_2/MgO and commercial 10 nm Fe_2O_3 catalysts; (b) Mg 2p XPS spectra of χ-Fe_5C_2/MgO and MgO.

Electron donors such as Na and K[15, 44-50] are well-known electronic promotors to boost olefin selectivity in CO/CO_2 hydrogenations. Besides, heteroatom-decorated carbon materials, such as N-doped graphene,[51, 52] N-doped carbon nanotubes[53] and N-doped carbon spheres[54] were also used to improve the olefin selectivity due to the extraordinary electron-donating ability of the N-doped functional groups in the carbon skeleton. Given the absence of Na and K in the as-prepared catalyst, we evidenced that the alkaline-earth metal oxide MgO, as a support, also behaved as an electron-donor for active metals. The electron-donating property of MgO is expected to be ascribed to its intrinsic basicity.

Mössbauer spectra and FFT analysis of HR-TEM of χ-Fe_5C_2/MgO (Fig. 1b, Table S1 and Fig. 3) confirm that the active phase is exclusively made up of Fe_5C_2 (96.9% Fe_5C_2 + 3.1% FeOx). Hereby, a model of Fe_5C_2 was built for DFT calculation as described in the Computational Methods section. According to the charge analysis, 0.26 electrons could be transferred from MgO to Fe_5C_2. The electron-donating ability of MgO has been well-documented in literature. Mckenna et al. deemed that the intriguing electronic properties of MgO could be ascribed to surface dislocations as well as surface defects, such as steps, kinks, and vacancies.[55]

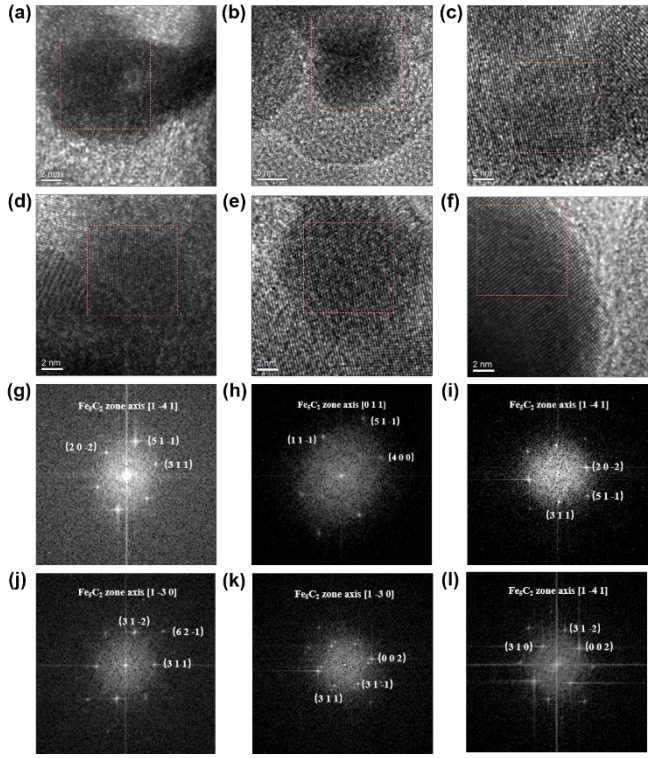

Fig. 3 HR-TEM image of (a) 20 h-χ-Fe_5C_2/MgO, (b) 50 h-χ-Fe_5C_2/MgO, (c) 20 h-p-χ-Fe_5C_2-MgO, (d) 50 h-p-χ-Fe_5C_2-MgO, (e) 20 h-p-χ-Fe_5C_2-SiC, (f) 50 h-p-χ-Fe_5C_2-SiC; (g-l): fast Fourier transformation (FFT) of selected area by red square in Fig. 3a-3f, respectively. Scale bar: (a) and (c-f), 2 nm; (b), 5nm.

Adsorption/Desorption of CO and H_2. The modification in electronic properties may vary adsorption/desorption behaviour of reactants, intermediate species, and products, thus giving rise to discrepancy in catalytic performance.[56, 57] To characterize the chemical adsorption properties of the catalysts, TPD of CO, H_2 and C_3H_6, was taken to explore the interactions between catalysts surfaces and reactants/products. The CO-TPD profile of χ-Fe_5C_2/MgO in Fig. 4a exhibits the highest CO desorption temperature at 587 °C, followed by p-χ-Fe_5C_2-MgO (450 °C), p-χ-Fe_5C_2-SiC (427 °C). The chemisorption of CO on catalysts surfaces is mainly due to the interaction of 5σ (HOMO) and 2π* (LUMO) orbitals of CO with the d-band of active metal according to frontier orbital theory proposed by Fukui.[58-61] The electron-donating effects induced by MgO increases the electron density of d-band of iron, thus promoting the electron transfer from d-band of Fe to 2π* (LUMO) orbital of CO. Consequently, more electrons in the 5σ (HOMO) orbital of CO are driven to fill the empty orbitals in the d-band of Fe.[62] The interaction between CO and the χ-Fe_5C_2 surface was enhanced due to the strengthened d-π feedback derived from extra electrons provided by MgO. As a result, the carbon-oxygen bond in CO was weakened, and the adsorption strength of CO on the χ-Fe_5C_2 surface was reinforced.

Desorption profiles of H_2 on various catalysts were also studied. The desorption temperature of H_2 (440 °C) for χ-

Fe_5C_2/MgO (Fig. 4b) is the lowest compared with that for p-χ-Fe_5C_2-MgO and p-χ-Fe_5C_2-SiC, implying the weakest H_2 adsorption on χ-Fe_5C_2/MgO. Our previous work has demonstrated that H_2 could adsorb on the surface competitively with CO and other species.[63] Therefore, the adsorption of H_2 on surface is expected to be weakened, given that CO adsorption is promoted on χ-Fe_5C_2/MgO. Li et al.[64] found that H_2 adsorption on surface Fe sites could be suppressed with the addition of MgO, and became more strongly with the increase of MgO amount. The attenuated H_2 adsorption may be attributed to the enhanced Pauli repulsion between the surface electrons and the approaching H_2, which is induced by MgO.[65]

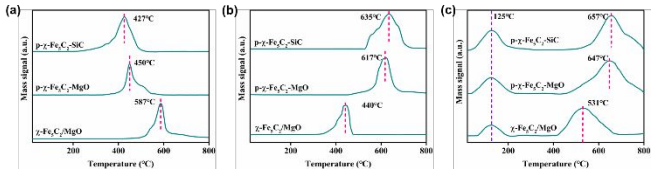

Fig. 4 (a) CO-TPD, (b) H_2-TPD and (c) C_3H_6-TPD profiles of p-χ-Fe_5C_2-SiC, p-χ-Fe_5C_2-MgO and χ-Fe_5C_2/MgO.

Adsorption/Desorption and Reactivity of Olefins. Secondary adsorption and hydrogenation reaction of olefins exerts adverse effects on the final olefin selectivity. The re-adsorption of olefin has proven to form more heavier hydrocarbons.[66-68] Gu et al. reported that the selectivity to α-olefins was promoted due to the impaired secondary olefin hydrogenation by co-feeding carboxylic acids.[69] Since propene (C_3H_6) accounts for the majority of lower olefins products (Table 1), C_3H_6-TPD was performed to examine the adsorption/desorption properties of olefins on catalyst surfaces while a pulse-C_3H_6 hydrogenation experiment was conducted to study the hydrogenation of olefins.

Two primary desorption peaks of C_3H_6 appeared in Fig. 4c, where the high temperature desorption peaks are associated with the strongly absorbed C_3H_6 and the low temperature desorption peaks are associated with the weakly absorbed ones. There was nearly no temperature shift for the weakly adsorbed C_3H_6 peak at 125 °C among these three catalysts. Whereas, the minimal desorption temperature (531 °C) for the strongly adsorbed C3H6 peak was spotted for χ-Fe_5C_2/MgO compared with p-χ-Fe_5C_2-MgO (647 °C), p-χ-Fe_5C_2-SiC (657 °C). Furthermore, this desorption behaviour is consistent with the crystal orbital Hamilton population (COHP) analysis. Fig. 7 shows the COHP curves and corresponding integrated COHP curves (ICOHP) of C_3H_6 adsorption on χ-Fe_5C_2 and χ-Fe_5C_2/MgO. The positive (+), negative (-), and zero (0) COHP values represent antibonding, bonding, and non-bonding interaction, respectively. χ-Fe_5C_2/MgO (Fig. 5b) shows a weaker bonding and stronger antibonding interaction for C_3H_6 than χ-Fe_5C_2 (Fig. 5a), which indicates a weaker C_3H_6 adsorption on χ-Fe_5C_2/MgO. Furthermore, the ICOHP at the Fermi level for χ-Fe_5C_2/MgO (-3.3) is larger than that for χ-Fe_5C_2 (-3.8), suggesting the less stable C_3H_6 adsorption configuration on χ-Fe_5C_2/MgO. In line with the Dewar–Chatt–Duncanson model, the adsorption of olefins is described as the interaction between the surface z^2 band of the active metal and π_σ/π_σ^* of the olefins.[70] We deduce that the variation in olefin adsorption ability in this study is ascribed to the changes in the z^2 band of the iron by MgO.

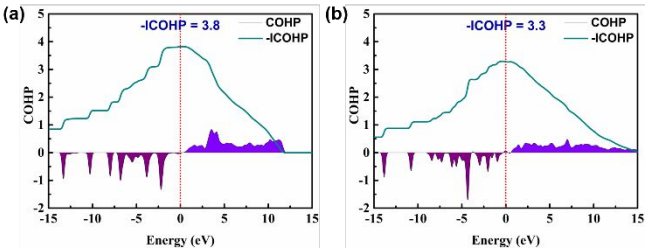

Fig. 5 COHP curves for C_3H_6 adsorption on (a) χ-Fe_5C_2 and (b) χ-Fe_5C_2/MgO, with the Fermi level set at zero, the dark cyan lines represent inversed integrated COHP (-ICOHP) for picture clarity, the -ICOHP up to the Fermi level is marked on the plots.

The reactivity of olefins was examined by the pulse-C_3H_6 hydrogenation transient analysis (Fig. 6). χ-Fe_5C_2/MgO exhibits the maximal R (peak intensity ratio of C_3H_6/C_3H_8 measured in MS) of 15.8, indicating its poorest olefin hydrogenation ability. It is noticed that R values for these three catalysts are larger than the ratio of C_3H_6/C_3H_8 (O/P of C_3 in Table 1) obtained from the catalytic performance (Table 1). Since PHTA was conducted under lower pressure (0.1 MPa) relative to the real reaction conditions (2.0 MPa), the adsorption and hydrogenation of olefins would be mitigated under lower operating pressure, which has been confirmed by kinetic studies. Meanwhile, the time interval between the occurrence of two consecutive peaks represents the retention time (RT) of olefins on surface. It is seen that χ-Fe_5C_2/MgO shows the shortest RT among all catalysts. This could be ascribed to the weakest olefin adsorption on χ-Fe_5C_2/MgO as presented in the C_3H_6-TPD profiles (Fig. 4c). The longer RT tends to lead to an increase in chain growth probability and lower O/P ratio in the product stream.[71] Combined with the H_2-TPD and C_3H_6-TPD profiles, we infer that the relative weak olefin hydrogenation activity for χ-Fe_5C_2/MgO is ascribed to its poor adsorption for H_2 and C_3H_6.

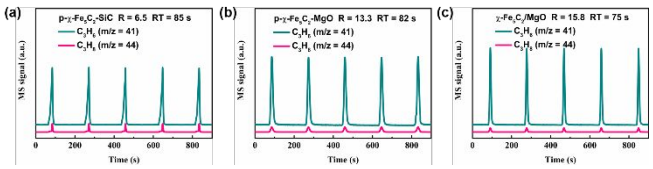

Fig. 6 Pulse-C_3H_6 Hydrogenation Transient Analysis of (a) p-χ-Fe_5C_2-SiC, (b) p-χ-Fe_5C_2-MgO and (c) χ-Fe_5C_2/MgO. R in the inserted legend represents the peak intensity ratio of C_3H_6 to corresponding C_3H_8; RT stands for the retention time of C_3H_6 on surface.

3.4 Critical role of MgO as a support

Size evolution of iron carbide and catalytic stability. As abovementioned, by altering the electronic properties of iron, MgO could enhance the adsorption of CO and decrease the adsorption of H_2 and C_3H_6, leading to the variation of ability in olefin hydrogenation. Besides, MgO exerts a geometric effect by dispersing iron species as well. Fig. S1 shows the XRD pattern of χ-Fe_5C_2/MgO after 50 h time on stream. As seen, no diffraction peaks related to iron species are detected. It is also worth noting that MgO is susceptible to transform into $MgCO_3$ or $Mg(OH)_2$ with CO_2 and H_2O generated during the reaction. While no $MgCO_3$ or $Mg(OH)_2$ was detected in the spent catalyst, indicating that MgO support is chemically stable under reaction conditions.

To explore the geometric evolution of different catalysts in detail, the TEM images were taken for the spent catalysts over 20 h and 50 h time on stream (Fig. 7). The size of χ-Fe_5C_2 for these three catalysts varies considerably from 20 h to 50 h. The average particle size of χ-Fe_5C_2 in χ-Fe_5C_2/MgO was increased by 2.2 nm (from 8.4 nm to 10.6 nm), which is much smaller than those in p-χ-Fe_5C_2-MgO (13.3 nm, from 8.7 nm to 22.0 nm) and p-χ-Fe_5C_2-SiC (14.0 nm, from 10.8 nm to 24.8 nm). Zhou et al.[72] proposed an Ostwald-ripening-like growth mechanism for the active iron carbides in FTS. According to their studies, the cyclic formation/deformation of iron carbonyl intermediates was the key factor affecting the size growth of iron species. The particle enlargement could be mitigated by suppressing the formation of iron carbonyl species with a high-N-content carbon support.[72] As mentioned before, N-doping was a popular method to functionalize carbon materials with electron-donating ability. Similarly, the particle growth for χ-Fe_5C_2/MgO is constrained, probably owing to the electron-donating effect of MgO support. As shown in Fig. 8 and Table 2, χ-Fe_5C_2/MgO showed a lower olefins selectivity of 57.4% at a CO conversion of 25.8% at 50 h, which nearly remains unchanged compared with that at 20 h. While the evident loss of CO conversion along with slightly-reduced olefin selectivity was observed for both p-χ-Fe_5C_2-MgO and p-χ-Fe_5C_2-SiC. The decreasing trend in activity and olefin selectivity with time-on-stream could be attributed to the reduction in the quantities of active sites caused by particle growth.[73]

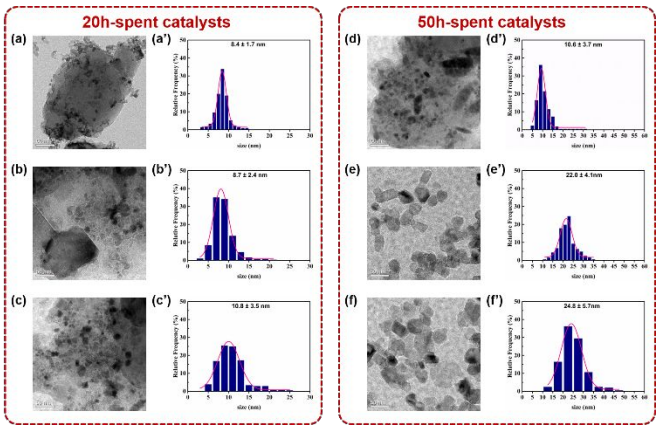

Fig. 7 (a), (b), (c): TEM images of 20h-spent χ-Fe_5C_2/MgO, p-χ-Fe_5C_2-MgO and p-χ-Fe_5C_2-SiC, respectively; (d), (e), (f): TEM images of 50 h-spent χ-Fe_5C_2/MgO, p-χ-Fe_5C_2-MgO and p-χ-Fe_5C_2-SiC, respectively; (a')-(f'): particle size distribution histograms of (a)-(f) with Gaussian analysis fittings, respectively. Scale bar: 50 nm.

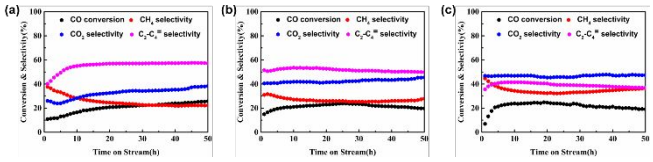

Fig. 8 The stability test of (a) χ-Fe_5C_2/MgO, (b) p-χ-Fe_5C_2-MgO and (c) p-χ-Fe_5C_2-SiC.

Table 2 Catalytic performance and particle size of χ-Fe_5C_2/MgO, p-χ-Fe_5C_2-MgO and p-χ-Fe_5C_2-SiC catalysts at different reaction time

Catalysts	χ-Fe_5C_2/MgO		p-χ-Fe_5C_2-MgO		p-χ-Fe_5C_2-SiC	
Reaction time (h)	20	50	20	50	20	50
CO conversion (%)	20.8	25.8	23.0	19.7	24.6	19.0
C_2-$C_4^=$ selectivity (%)	56.9	57.4	52.7	49.9	40.4	37.0
Iron particle size (nm)	8.4	10.6	8.7	22.0	10.8	24.8

Intimacy between χ-Fe_5C_2 and MgO. The intimacy criterion is commonly used to regulate the distance between two different active sites in the metal/acid bifunctional catalysts.[74]] The intimacy effect is also reported in the metal oxide-zeolites (OX-ZEO) bifunctional catalysts for syngas conversion to lower olefins.[75, 76]

In the present study, we also observed the effect of intimacy between χ-Fe_5C_2 and MgO on catalytic performance. As shown in Fig. 9, a series of Fe_2O_3-MgO catalysts with

controlled intimacy were prepared and evaluated. However, different from the optimal proximity commonly observed in the OX-ZEO process, we observed a "the closer the better" phenomenon. An obvious loss in olefin selectivity (from 57.4% to 44.0%) was accompanied with the further distance between iron and MgO. Han et al.[77] proposed that a medium distance between K_2CO_3 and Fe is better for CO_2 hydrogenation process. CO_2 hydrogenation is widely recognized as the combination of a reverse water gas shift (RWGS) and a FT process, consequently both Fe_3O_4 (active for RWGS) and iron carbide (active for FT) were indispensable for such a reaction. The authors deemed that a medium proximity was benefit for acquiring the proper Fe_3O_4 and χ-Fe_5C_2 proportion, thus, for the maximum olefin selectivity. However, it is widely accepted that Fe_3O_4 is not an active phase in the FT reaction. Combined with the fact that K_2CO_3 is more basic than MgO, we speculate that a closer interaction with Fe was required for MgO regarding with K_2CO_3 in achieving the highest olefin selectivity.

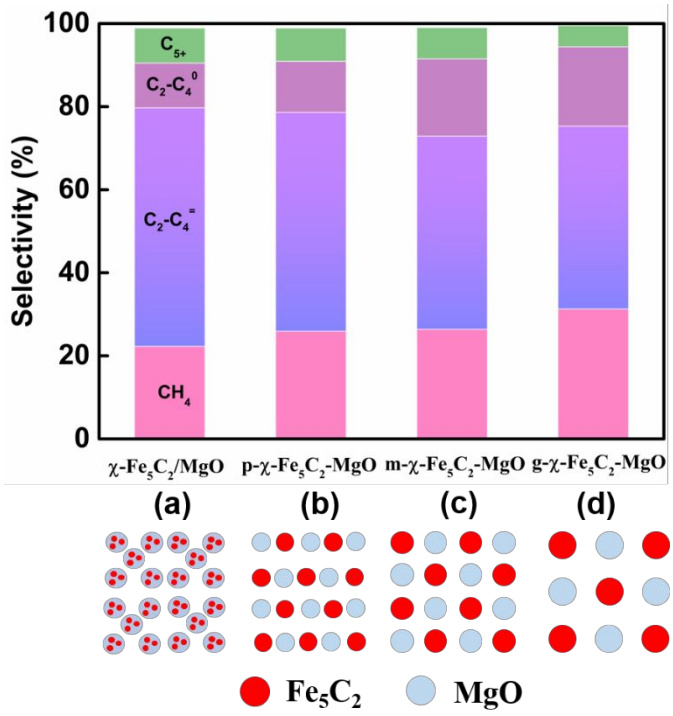

Fig. 9 CO hydrogenation performance over catalysts with different χ-Fe_5C_2 and MgO proximity. (a) χ-Fe_5C_2/MgO, and mechanical mixing of Fe_2O_3 and MgO with controlled granule size (b) powder mixing, ~10 μm, p-χ-Fe_5C_2-MgO, (c) 160~200 meshes, ~85.5 μm, m-χ-Fe_5C_2-MgO, (d) 20~40 meshes, ~605 μm, g-χ-Fe_5C_2-MgO.

χ-Fe_5C_2/MgO versus MgO/χ-Fe_5C_2. To further investigate the superior catalytic performance of the χ-Fe_5C_2/MgO catalyst, we have synthesized a series of MgO/Fe_2O_3 precursors by loading MgO on α-Fe_2O_3 (10 nm) nanoparticles. Both χ-Fe_5C_2/MgO and MgO/χ-Fe_5C_2 possess the same MgO and χ-Fe_5C_2 proximity, thus the difference in product selectivity and catalytic stability is mainly attributed to the supporting approaches.

Fig. 10 shows that the selectivity of lower olefins exhibits a volcano-type curve against the loadings of MgO, with the maximum of 56.2% C_2-C_4 olefin selectivity at 10% MgO/χ-Fe_5C_2. An increase in Mg loading from 5% to 10% may lead to the creation of more χ-Fe_5C_2 interface, thus leading to an enhancement in the olefin selectivity. Excess Mg loading (e.g., 20% MgO/χ-Fe_5C_2) probably forms a bulk MgO phase that block the active Fe site, causing an activity loss.

Besides, the deactivation behaviours vary for different MgO loading catalysts. A fast deactivation was observed for 5% MgO/χ-Fe_5C_2 at about 15 h, compared with 28 h for 10% MgO/χ-Fe_5C_2, 33 h for 20% MgO/χ-Fe_5C_2. The decoration of MgO may weaken the surface energy of Fe,[78] thus retarding the aggregation of iron carbide particles. However, such a decoration cannot guarantee a favourable stability, since all the MgO/χ-Fe_5C_2 catalysts deactivate within 50 h time on stream (Fig. 10).

Therefore, loading MgO on χ-Fe_5C_2 could indeed enhance the olefin selectivity and improve the catalyst durability to a limited extent. Meanwhile, compared with the favourable stability of χ-Fe_5C_2/MgO (Fig. 8a), the censorable stability of MgO/χ-Fe_5C_2 evidenced that the superiority of MgO lied in the bifunctional roles of an alkaline promoter and a stable support.

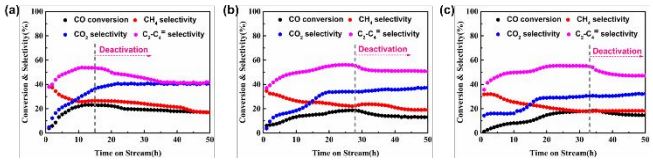

Fig. 10 CO hydrogenation performance over MgO/χ-Fe_5C_2 catalysts with different MgO loadings. (a) 5% MgO, (b) 10% MgO, (c) 20% MgO.

3.5 Effects of reaction conditions

Performance test of χ-Fe_5C_2/MgO under different reaction conditions (temperature, pressure and GHSV) was conducted to evaluate its industrial usability. As shown in Fig. 11a, a maximum C_2-C_4 olefin selectivity was obtained at 280 °C. The STO reaction is known as a temperature-sensitive process.[7] With the temperature increasing from 260 °C to 320 °C, the hydrogenation ability of the catalyst was enforced, yielding a higher methane and a lower C_{5+} selectivity. The reaction pressure and GHSV also exert changes to the activity and selectivity (Fig. 11b and 11c). The discrepancy on the products distribution mainly results from the change in CH_4 and C_{5+}. A higher reaction pressure results in a lower methane and a higher C_{5+} selectivity, accompanied with a higher CO conversion. A higher GHSV leads to a higher methane and a lower C_{5+} selectivity, along with a lower CO conversion.

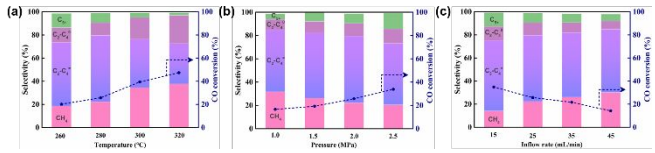

Fig. 11 CO hydrogenation performance over χ-Fe_5C_2/MgO under different reaction conditions. (a) temperature, (b) pressure, (c) GHSV, inflow rate.

3.6 Structure-performance relationship

The interaction between χ-Fe_5C_2 and MgO support follows an order of χ-Fe_5C_2/MgO > p-χ-Fe_5C_2-MgO> m-χ-Fe_5C_2-MgO > g-χ-Fe_5C_2-MgO >> p-χ-Fe_5C_2-SiC. The χ-Fe_5C_2/MgO catalyst, with the strongest χ-Fe_5C_2 and MgO interaction, exhibited the highest C_2-C_4 olefins selectivity (57.4%) over 50 h reaction time.

χ-Fe_5C_2/MgO shows a constant CO conversion and lower olefin selectivity over 50 h TOS (Fig. 8 and Table 2). In contrast, the other two iron catalysts prepared by powder mixing (p-χ-Fe_5C_2-MgO and p-χ-Fe_5C_2-SiC) presented obvious loss in activity and selectivity after 20 h. It is also noted that the powder mixed catalyst p-χ-Fe_5C_2-MgO showed a medium performance. Considering the catalyst was activated at a relatively high temperature (350 °C), a weaker χ-Fe_5C_2 and MgO interaction is expected for p-χ-Fe_5C_2-MgO, thus offering higher performance than p-χ-Fe_5C_2-SiC which has no interaction between χ-Fe_5C_2 and MgO. Consequently, the superiority of χ-Fe_5C_2/MgO can be illustrated as Scheme 1. The dual roles of MgO are assumed as: (1) enables the dispersion and stabilization of the χ-Fe_5C_2 nanoparticles during reaction; (2) acts as an electron donor to χ-Fe_5C_2. Owing to such a bifunctional characteristic, the active sites of the supported Fe catalysts can be maintained at a high level for a long time, thus giving rise to a high selectivity to C_2-C_4 olefins at long-time stability.

The electron transfer from MgO to Fe has been confirmed by XPS analysis of the as-prepared χ-Fe_5C_2/MgO (Fig. 2). The improvements in electronic properties have proved to enhance CO dissociation and suppress H_2 adsorption, adsorption, and hydrogenation of olefins, which are confirmed by both TPD measurements (Fig. 4) and COHP analysis from DFT calculation (Fig. 5). Those factors are favourable for a high olefin selectivity. χ-Fe_5C_2/MgO outperformed the physically mixed MgO and χ-Fe_5C_2, suggesting that the closer proximity of χ-Fe_5C_2 to the electron-rich MgO support in χ-Fe_5C_2/MgO improves the electron transfer. Thus, we argue that the relatively high olefin selectivity may be ascribed to the electronic effect of MgO.

On the other hand, the diffraction features of MgO in XRD patterns over both the precursor and χ-Fe_5C_2/MgO, suggesting that MgO can enhance the dispersion of iron oxide particles, which could suppress the particle growth during the reaction (Table 2). Although the MgO/χ-Fe_5C_2 catalyst exhibits an enhanced olefin selectivity, the catalyst deactivates gently within 50 h time on stream. In contrast, χ-Fe_5C_2/MgO shows an exceptional stability over 50 h time on stream. Therefore, MgO plays an essential role in obtaining a high stability when used as a catalyst support rather than as a promoter.

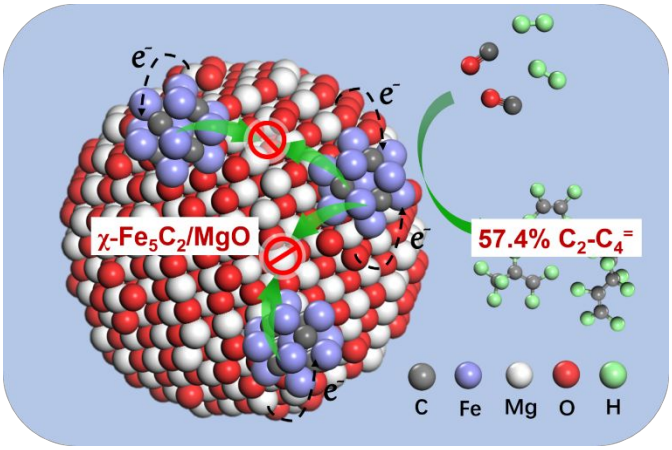

Scheme 1 Scheme for the bifunctional roles of MgO for χ-Fe_5C_2/MgO for STO.

Conclusions

The interaction between MgO support and χ-Fe_5C_2 have proved to impose profound effects on the physicochemical properties of iron catalysts for lower olefins synthesis directly from syngas. The interaction between χ-Fe_5C_2 and MgO is essential to increase the selectivity to olefins. The combination of in situ XPS, TPD spectra and DFT calculation have demonstrated the electron transfer from MgO to Fe species, which is responsible for the production of olefins. On the other hand, TEM images revealed that MgO could disperse and stabilize the iron species and constrain the growth of iron carbide particles. Therefore, the benefits of MgO lie in both structural and electronic modification of the active iron species, giving rise to a high selectivity towards lower olefin and exceptional stability. This contribution confirms the feasibility of promoting the olefin selectivity and stability of the existing iron-based STO catalyst with MgO support.

Author Contributions

Yitao Liu: investigation, formal analysis, writing original draft, review & editing. Xianglin Liu: theoretical calculation. Zixu Yang: investigation, review & editing. Hu Li: investigation, formal analysis. Xiaoxu Ding: investigation, formal analysis. Minjie Xu: formal analysis. Xinli Li: investigation. Wei-Feng Tu: data curation. Minghui Zhu: review & editing. Yi-Fan Han: review & editing, supervision, project administration.

Conflicts of interest

There are no conflicts to declare.

Acknowledgements

The authors greatly acknowledge the funding support from National Science Foundation (21878080), Shanghai Sailing Program (19YF1411000), China Postdoctoral Science Foundation (2018M641034), Fundamental Research Funds for the Central Universities (222201814006) and Ningxia Science Foundation (2019AAC03282).

References

1 R. Zennara, 2013.
2 H. M. Torres Galvis and K. P. de Jong, ACS Catal., 2013, 3, 2130-2149.
3 P. Tian, Y. Wei, M. Ye and Z. Liu, ACS Catal., 2015, 5, 1922-1938.
4 Z. L. Guangyu Cai, Renmin Shi, Changqing He, Lixin Yang, Chenglin Sun, Yanjun Chang, Appl. Catal., A, 1995, 125, 29-38.
5 H. M. Torres Galvis, J. H. Bitter, C. B. Khare, M. Ruitenbeek, A. I. Dugulan and K. P. de Jong, Science 2012, 335, 835-838.
6 Y. An, T. Lin, F. Yu, Y. Yang, L. Zhong, M. Wu and Y. Sun, Sci. China: Chem., 2017, 60, 887-903.
7 J. van de Loosdrecht, F. G. Botes, I. M. Ciobica, A. Ferreira, P. Gibson, D. J. Moodley, A. M. Saib, J. L. Visagie, C. J. Weststrate and J. W. Niemantsverdriet, 2013.
8 K. Cheng, J. Kang, D. L. King, V. Subramanian, C. Zhou, Q. Zhang and Y. Wang, in Adv. Catal., ed. C. Song, 2017, vol. 60, pp. 125-208.
9 P. J. Flory, J. Am. Chem. Soc., 1936, 58, 1877-1885.
10 G. Henrici-Olivé and S. Olivé, Angew. Chem., Int. Ed., 1976, 15, 136-141.
11 E. de Smit and B. M. Weckhuysen, Chem. Soc. Rev., 2008, 37, 2758-2781.
12 H. Suo, S. Wang, C. Zhang, J. Xu, B. Wu, Y. Yang, H. Xiang and Y.-W. Li, J. Catal., 2012, 286, 111-123.
13 H.-J. Wan, B.-S. Wu, C.-H. Zhang, H.-W. Xiang, Y.-W. Li, B.-F. Xu and F. Yi, Catal. Commun., 2007, 8, 1538-1545.
14 A. C. J. Koeken, H. M. Torres Galvis, T. Davidian, M. Ruitenbeek and K. P. de Jong, Angew. Chem., Int. Ed., 2012, 51, 7190-7193, S7190/7191-S7190/7120.
15 Y. Cheng, J. Lin, K. Xu, H. Wang, X. Yao, Y. Pei, S. Yan, M. Qiao and B. Zong, ACS Catal., 2016, 6, 389-399.
16 Y. Ono, J. Catal., 2003, 216, 406-415.
17 L.-B. Sun, X.-Q. Liu and H.-C. Zhou, Chem. Soc. Rev., 2015, 44, 5092-5147.
18 S. Badoga, G. Kamath and A. Dalai, Applied Catalysis A: General, 2020, 607, 117861.
19 Y. Zhang, H. Xiong, K. Liew and J. Li, Journal of Molecular Catalysis A: Chemical, 2005, 237, 172-181.
20 A. Nakhaei Pour, S. M. K. Shahri, H. R. Bozorgzadeh, Y. Zamani, A. Tavasoli and M. A. Marvast, Applied Catalysis A: General, 2008, 348, 201-208.
21 S. Zhang, N. J. Marriott and W. E. Lee, J. Eur. Ceram. Soc., 2001, 21, 1037-1047.
22 S. Zhang and W. E. Lee, J. Eur. Ceram. Soc., 2001, 21, 2393-2405.
23 G. Kresse and J. Furthmüller, Comput. Mater. Sci., 1996, 6, 15-50.
24 J. P. Perdew and A. Zunger, Phys. Rev. B, 1981, 23, 5048-5079.
25 J. P. Perdew, K. Burke and M. Ernzerhof, Phys. Rev. Lett., 1996, 77, 3865-3868.
26 J. Baltrusaitis, C. Hatch and R. Orlando, J. Phys. Chem. A 2012, 116, 7950-7958.
27 R. S. Alvim, I. Borges, D. G. Costa and A. A. Leitão, J. Phys. Chem. C 2012, 116, 738-744.
28 T. H. Pham, Y. Qi, J. Yang, X. Duan, G. Qian, X. Zhou, D. Chen and W. Yuan, ACS Catal., 2015, 5, 2203-2208.
29 B. Chen, D. Wang, X. Duan, W. Liu, Y. Li, G. Qian, W. Yuan, A. Holmen, X. Zhou and D. Chen, ACS Catal., 2018, 8, 2709-2714.
30 Y. Liu, F. Lu, Y. Tang, M. Liu, F. F. Tao and Y. Zhang, Appl. Catal., B, 2020, 261, 118219.
31 Y. Zhang, D. Fu, X. Liu, Z. Zhang, C. Zhang, B. Shi, J. Xu and Y.-F. Han, ChemCatChem, 2018, 10, 1272-1276.
32 J. Xie, G. H. M. Torres, J. K. P. de, A. C. J. Koeken, A. Kirilin, M. Ruitenbeek and A. I. Dugulan, ACS Catal., 2016, 6, 4017-4024.
33 H. M. Torres Galvis, J. H. Bitter, T. Davidian, M. Ruitenbeek, A. I. Dugulan and K. P. de Jong, J. Am. Chem. Soc., 2012, 134, 16207-16215.
34 K.-D. J. Eun-Ku Lee, Oh-Shim Joo, Yong-Gun Shul, Bull. Korean Chem. Soc., 2005, 26.
35 W. Zhang, H. L. Tay, S. S. Lim, Y. Wang, Z. Zhong and R. Xu, Appl. Catal., B, 2010, 95, 93-99.
36 W. Kündig, H. Bömmel, G. Constabaris and R. H. Lindquist, Phys. Rev., 1966, 142, 327-333.
37 J. K. Norskov, T. Bligaard, J. Rossmeisl and C. H. Christensen, Nat. Chem., 2009, 1, 37-46.
38 G. Chen, C. Xu, X. Huang, J. Ye, L. Gu, G. Li, Z. Tang, B. Wu, H. Yang, Z. Zhao, Z. Zhou, G. Fu and N. Zheng, Nat. Mater., 2016, 15, 564-569.
39 J. K. Nørskov, T. Bligaard, A. Logadottir, S. Bahn, L. B. Hansen, M. Bollinger, H. Bengaard, B. Hammer, Z. Sljivancanin, M. Mavrikakis, Y. Xu, S. Dahl and C. J. H. Jacobsen, J. Catal., 2002, 209, 275-278.
40 P. B. Weisz, J. Phys. Chem., 1953, 21, 1531-1538.
41 J. K. Nørskov, Natl. Sci. Rev., 2015.
42 Z. Zhang, J. Zhang, X. Wang, R. Si, J. Xu and Y.-F. Han, Journal of Catalysis, 2018, 365, 71-85.
43 C. Zhang, M. Xu, Z. Yang, M. Zhu, J. Gao and Y.-F. Han, Applied Catalysis B: Environmental, 2021, 295, 120287.
44 P. Zhai, M. Li, W. Li, J. Xie, D. Ma, C. Xu, M. Zhao, Q. Zhang, R. Gao, X. Liu, X. Wang, Y.-W. Li, X.-D. Wen, R. Gao, X. Liu, X. Wang, Y.-W. Li, X.-D. Wen, X. Fu and C. Jia, Angew. Chem., Int. Ed., 2016, 55, 9902-9907.
45 Z. J. Li, L. S. Zhong, F. Yu, Y. L. An, Y. Y. Dai, Y. Z. Yang, T. J. Lin, S. G. Li, H. Wang, P. Gao, Y. H. Sun and M. Y. He, ACS Catal., 2017, 7, 3622-3631.
46 H. M. Torres Galvis, A. C. J. Koeken, J. H. Bitter, T. Davidian, M. Ruitenbeek, A. I. Dugulan and K. P. de Jong, J. Catal., 2013, 303, 22-30.
47 C. F. Huo, B. S. Wu, P. Gao, Y. Yang, Y. W. Li and H. Jiao, Angew. Chem., Int. Ed., 2011, 50, 7403-7406.
48 A. P. Raje, R. J. O'Brien and B. H. Davis, J. Catal., 1998, 180, 36-43.
49 Y. Cheng, J. Tian, J. Lin, S. Wang, S. Xie, Y. Pei, S. Yan, M. Qiao, H. Xu and B. Zong, J. Catal., 2019, 374, 24-35.
50 Y. H. Choi, E. C. Ra, E. H. Kim, K. Y. Kim, Y. J. Jang, K.-N. Kang, S. H. Choi, J.-H. Jang and J. S. Lee, ChemSusChem, 2017, 10, 4764-4770.
51 X. Chen, D. Deng, X. Pan, Y. Hu and X. Bao, Chem. Commun. , 2015, 51, 217-220.
52 Y. S. Yun, H. Park, D. Yun, C. K. Song, T. Y. Kim, K. R. Lee, Y. Kim, J. W. Han and J. Yi, Chem. Commun. , 2018, DOI: 10.1039/c8cc03107j.
53 J. Lu, L. Yang, B. Xu, Q. Wu, D. Zhang, S. Yuan, Y. Zhai, X. Wang, Y. Fan and Z. Hu, ACS Catal., 2014, 4, 613-621.

54 H. Xiong, M. Moyo, M. A. Motchelaho, Z. N. Tetana, S. M. A. Dube, L. L. Jewell and N. J. Coville, J. Catal., 2014, 311, 80-87.
55 K. P. McKenna, J. Am. Chem. Soc., 2013, 135, 18859-18865.
56 A. Nilsson, L. G. M. Pettersson, B. Hammer, T. Bligaard, C. H. Christensen and J. K. Norskov, Catal. Lett., 2005, 100, 111-114.
57 J. K. Norskov, T. Bligaard, B. Hvolbaek, F. Abild-Pedersen, I. Chorkendorff and C. H. Christensen, Chem. Soc. Rev., 2008, 37, 2163-2171.
58 K. Fukui, T. Yonezawa and H. Shingu, J. Phys. Chem., 1952, 20, 722-725.
59 K. Fukui, Acc. Chem. Res., 1971, 4, 57-64.
60 K. Fukui, Science, 1982, 218, 747-754.
61 K. Fukui, J. Phys. Chem., 1970, 74, 4161-4163.
62 G. Blyholder, J. Phys. Chem., 1964, 68, 2772-2777.
63 Z. Zhang, W. Dai, X.-C. Xu, J. Zhang, B. Shi, J. Xu, W. Tu and Y.-F. Han, AIChE J., 2017, 63, 4451-4464.
64 J. Li, C. Zhang, X. Cheng, M. Qing, J. Xu, B. Wu, Y. Yang and Y. Li, Appl. Catal., A, 2013, 464-465, 10-19.
65 J. Harris and S. Andersson, Phys. Rev. Lett., 1985, 55, 1583-1586.
66 R. J. Madon and E. Iglesia, J. Catal., 1993, 139, 576-590.
67 E. W. Kuipers, I. H. Vinkenburg and H. Oosterbeek, J. Catal., 1995, 152, 137-146.
68 M. C. Hans Schulz, Appl. Catal., A, 1999.
69 B. Gu, A. Y. Khodakov and V. V. Ordomsky, Chem. Commun. , 2018, 54, 2345-2348.
70 G. J. Kubas, J. Organomet. Chem., 2001, 635, 37-68.
71 E. Iglesia, S. C. Reyes and R. J. Madon, J. Catal., 1991, 129, 238-256.
72 O. Zhuo, L. Yang, F. Gao, B. Xu, Q. Wu, Y. Fan, Y. Zhang, Y. Jiang, R. Huang, X. Wang and Z. Hu, Chem. Sci., 2019, 10, 6083-6090.
73 A. K. Datye, Y. Jin, L. Mansker, R. T. Motjope, T. H. Dlamini and N. J. Coville, in Stud. Surf. Sci. Catal., eds. A. Corma, F. V. Melo, S. Mendioroz and J. L. G. Fierro, Elsevier, 2000, vol. 130, pp. 1139-1144.
74 P. B. Weisz, in Advances in Catalysis, eds. D. D. Eley, P. W. Selwood, P. B. Weisz, A. A. Balandin, J. H. De Boer, P. J. Debye, P. H. Emmett, J. Horiuti, W. Jost, G. Natta, E. K. Rideal and H. S. Taylor, Academic Press, 1962, vol. 13, pp. 137-190.
75 F. Jiao, J. Li, X. Pan, J. Xiao, H. Li, H. Ma, M. Wei, M. Li, S. Miao, J. Li, Y. Zhu, D. Xiao, T. He, J. Yang, Q. Fu, X. Bao, Y. Pan, Z. Zhou and F. Qi, Science, 2016, 351, 1065-1068.
76 K. Cheng, B. Gu, X. Liu, J. Kang, Q. Zhang and Y. Wang, Angewandte Chemie International Edition, 2016, 55, 4725-4728.
77 Y. Han, C. Fang, X. Ji, J. Wei, Q. Ge and J. Sun, ACS Catalysis, 2020, 10, 12098-12108.
78 C. T. Campbell, Acc. Chem. Res., 2013, 46, 1712-1719.